SAND2008-3070C

DUAL-PERMEABILITY MODELING AND EVALUATION OF DRIFT-SHADOW EXPERIMENTS

Clifford K. Ho, Bill W. Arnold, and Susan J. Altman

Sandia National Laboratories, P.O. Box 5800, Albuquerque, NM 87185-0735, ckho@sandia.gov

The drift-shadow effect describes capillary diversion of water flow around a drift or cavity in porous or fractured rock, resulting in lower water flux directly beneath the cavity. This paper presents computational simulations of drift-shadow experiments using dual-permeability models, similar to the models used for performance assessment analyses of flow and seepage in unsaturated fractured tuff at Yucca Mountain. Results show that the dual-permeability models capture the salient trends and behavior observed in the experiments, but constitutive relations (e.g., fracture capillary-pressure curves) can significantly affect the simulated results. An evaluation of different meshes (orthogonal vs. unstructured) is also presented..

I. INTRODUCTION

Previous tests using X-ray absorption imaging have provided quantitative and visual evidence of the drift-shadow effect in unsaturated fractured tuff.[1] The drift-shadow effect includes capillary diversion of water flow around a drift or cavity, resulting in lower water flux directly beneath the cavity. This paper presents simulations of these tests using dual-permeability models, similar to the models used for performance assessment analyses of flow and seepage in unsaturated fractured tuff at Yucca Mountain. Previous analytical solutions have been developed to predict the drift-shadow effect in porous media[2], and Houseworth et al.[3] developed a dual-permeability model of flow diversion around a simulated drift at Yucca Mountain in unsaturated fractured tuff. However, no experimental or field data were available for comparison to the theoretical results in those studies.

The purpose of this study is to present an evaluation of flow diversion and drift-shadow effects observed in experiments performed by Altman et al.[1] using a dual-permeability model. Alternative model parameters and modeling methods are investigated to determine the potential impact on simulated results.

II. EXPERIMENTAL SUMMARY

In the experiments performed by Altman et al.,[1] two machined slabs of Topopah Spring welded tuff were separated by thin wires to represent desired fracture apertures. An ~8 cm diameter circular hole cut through the slabs represented an open drift in the tuff. The slabs were held in place with an aluminum frame and encased with epoxy and Plexiglass. Water was introduced at prescribed flow rates through inflow ports at four locations along the top of the fracture aperture. The flow was allowed to reach steady-state, and the outflow was collected in five bins along the bottom of the apparatus to determine the flux distribution pattern below the drift. X-ray imaging was used to visualize solute (potassium iodide) flow paths through the fracture and tuff matrix during the experiment. Figure 1 shows a schematic of the tuff samples and test cell. Additional details of the experimental apparatus and test procedure can be found in Altman et al.[1]

Figure 2 shows some results from the 500-micron aperture experiments using X-ray imaging. The solute flow paths are distinct and appear to follow discrete "fingers" through the fracture aperture. In addition, the solute appears to be diverted around the drift opening. Heterogeneities in the tuff slabs (higher porosity pumice fragments) appear to increase the diffusion or imbibition of the solute into the tuff matrix. Locations with pumice fragments show up as "hot spots" in the X-ray images. However, it is unclear if these heterogeneities in the matrix affected the distribution of flow in the fracture aperture. The distribution of outflow beneath the drift cavity is discussed along with a comparison to the models in Section IV.

III. COMPUTATIONAL APPROACH

The dual-permeability model has been used to model flow and transport within fractured rock at Yucca Mountain.[4] In this conceptual model, flow and transport can occur through both the fracture and matrix continua, as well as between the fracture and matrix continua.[5] Although a single-continuum fracture model would probably suffice for the test conditions implemented in Altman et al.[1], dual-permeability models of the experiments were developed because it was desired to replicate the models used on the Yucca Mountain project.

Both TOUGH2[6] and FEHM[7] were used in the numerical simulations of the drift-shadow experiments, and both codes have been used to simulate flow and transport for the Yucca Mountain project. TOUGH2 has also been used to simulate seepage into drifts and mountain-scale drift-shadow effects on flow and transport.[3] Section III.A describes the different applications of these codes for this work and the computational domain. Sections III.B and III.C describe the properties, and boundary conditions used in the models.

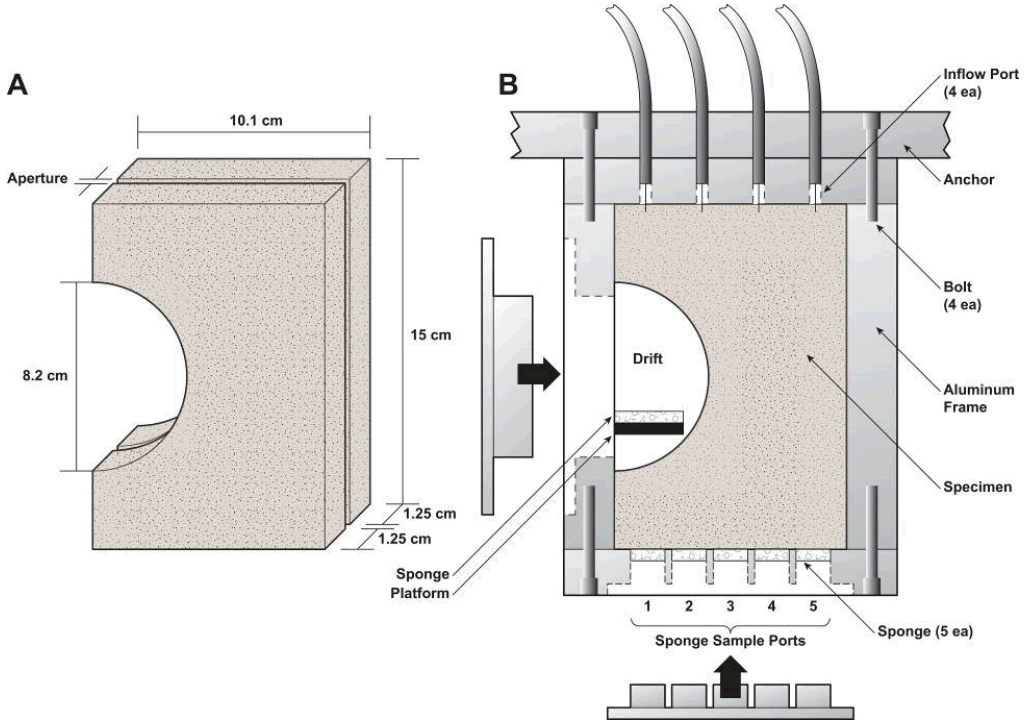

Figure 1. Schematic of (A) tuff slabs and (B) test cell used in Altman et al.[1] (with permission from Elsevier).

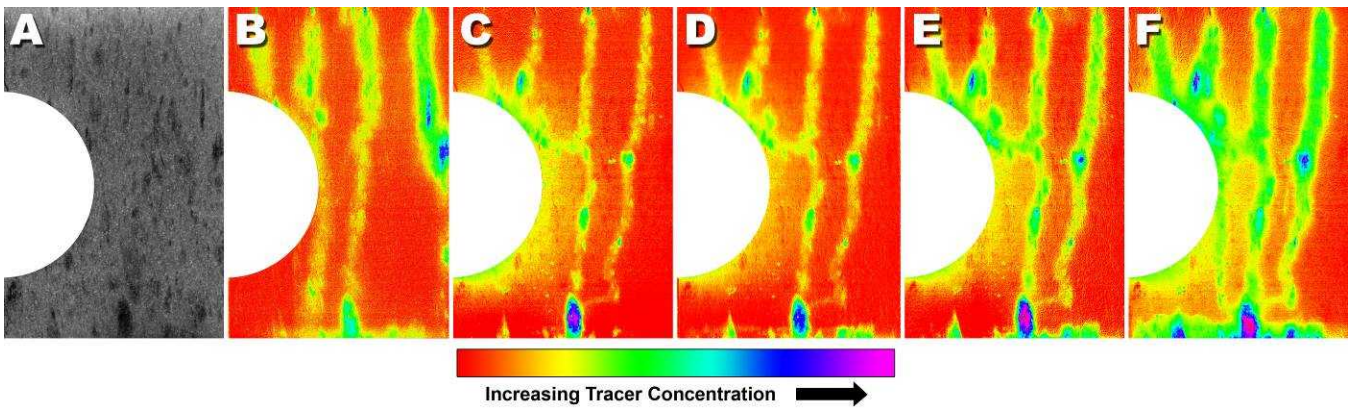

Figure 2. X-ray absorption images of the 500-micron aperture test cell taken (A) before and (B) 5 h after the start of experiment at 0.01 ml/min and (C) 1, (D) 2, (E) 3, and (F) 5 h after start of experiment with 0.23 ml/min flow rate. Image of cell without tracer (A) shows porous pumice fragments as darker areas. From Altman et al.[1] (with permission from Elsevier).

III.A. Computational Domain

The domain of the drift-shadow experiment was represented with a uniform orthogonal mesh consisting of 3220 fracture elements and 3220 matrix elements, all interconnected (Figure 3a). The resolution of the mesh was sufficient to capture capillary diversion and drift-shadow effects at the scale of the experiments. The benefits of using an orthogonal mesh include minimizing the numerical dispersion when the elements are aligned in the direction of flow and improved computational convergence. However, for non-orthogonal features, such as the circular drift, the use of orthogonal elements creates a stair-stepped interface that may artificially increase the capillary pressure required to divert water around the drift. Therefore, an alternative mesh was generated using an unstructured Voronoi grid with 3201 primary elements (Figure 3b). The impact of the grids on the flow distribution around the drift is investigated in Section IV.C.

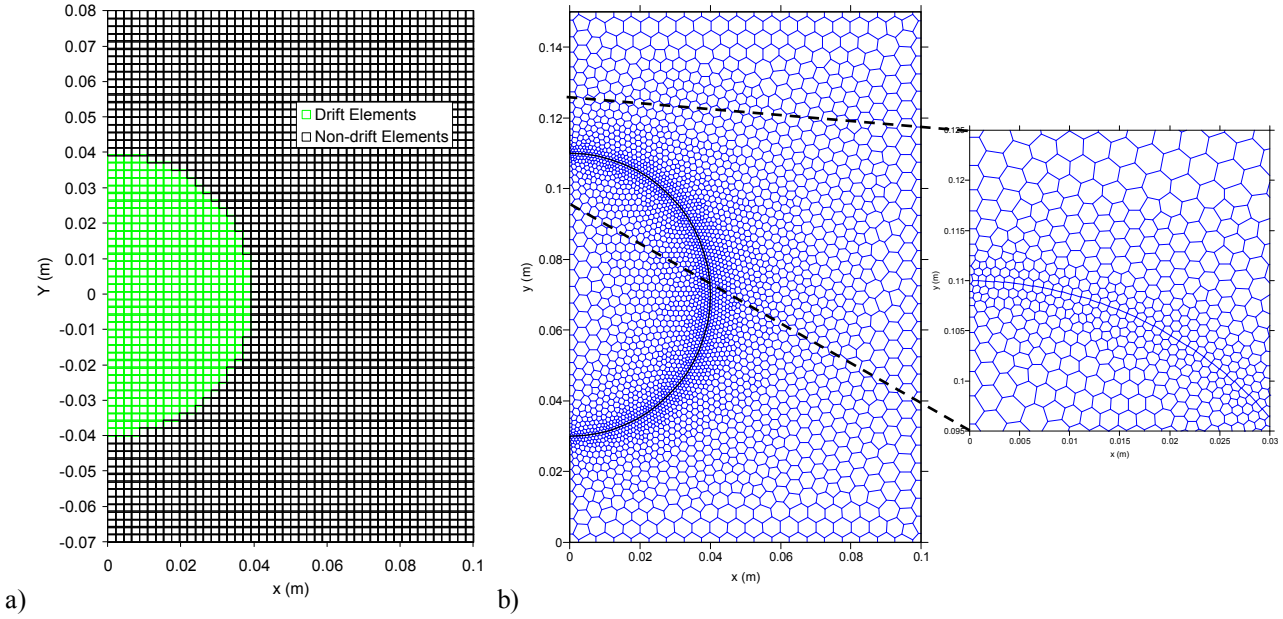

Figure 3. Computational meshes used in the simulations. a) orthogonal mesh used in TOUGH2 simulations, b) unstructured Voronoi mesh used in FEHM simulations.

III.B. Hydraulic Properties

Hydraulic properties of the fracture and matrix continua simulated in the dual-permeability models are summarized in Table 1. The matrix properties were based on values published by Flint[8] for samples of Topopah Spring Tuff in the lithophysal zone. The matrix van Genuchten α and n parameters were obtained using these matrix properties together with regressions from Altman.[9]

The bulk fracture porosity, ϕ_f, permeability, k_f, and van Genuchten α_f parameter were calculated as follows:

$$\phi_f = b/D \tag{1}$$

$$k_f = \frac{b^2}{12}\phi_f \tag{2}$$

$$\alpha = \frac{b\rho g}{2\sigma \cos\theta} \tag{3}$$

where b is the fracture aperture[m], D is the fracture spacing [0.025 m], ρ is the liquid density [998 kg/m^3 at 20ºC], g is the gravitational constant [9.81 m/s^2], σ is the surface tension of liquid water [0.072 N/m at 20ºC], and θ is the contact angle (assumed to be zero). Eq. (1) assumes one-dimensional planar fractures. Eq. (2) assumes laminar, fully developed, incompressible flow between two parallel planes, and Eq. (3) is derived from capillary pressure and force balance considerations at a liquid/air interface (Young-Laplace equation).

Table 1. Summary of hydraulic properties used in dual-permeability models.

Parameter	Value	Ref.
Matrix porosity [-]	0.154	8
Matrix permeability [m^2]	$8.9x10^{-18}$	8
Matrix van Genuchten α [Pa^{-1}]	$1.82x10^{-6}$	9
Matrix van Genuchten n [-]	1.6	9
Fracture porosity, 100 μm aperture [-]	0.004	Eq. (1)
Fracture bulk permeability, 100 μm aperture [m^2]	$3.32x10^{-12}$	Eq. (2)
Fracture van Genuchten α, 100 μm aperture [Pa^{-1}]	$6.94x10^{-4}$	Eq. (3)
Fracture porosity, 250 μm aperture [-]	0.0099	Eq. (1)
Fracture bulk permeability, 250 μm aperture [m^2]	$5.16x10^{-11}$	Eq. (2)
Fracture van Genuchten α, 250 μm aperture [Pa^{-1}]	$1.73x10^{-3}$	Eq. (3)
Fracture porosity, 500 μm aperture [-]	0.0196	Eq. (1)
Fracture bulk permeability, 500 μm aperture [m^2]	$4.08x10^{-10}$	Eq. (2)
Fracture van Genuchten α, 500 μm aperture [Pa^{-1}]	$3.47x10^{-3}$	Eq. (3)
Fracture van Genuchten n, all apertures [-]	3.0	9

III.C. Boundary Conditions

Three different fracture apertures were prescribed for the tests: 100, 250, and 500 microns. For each of the prescribed apertures, different flow rates were introduced at four locations along the top of the fracture aperture through a needle (see Figure 1). Table 2 summarizes the different injection rates for the different apertures. Only the low and high injection rates used in the experiments were simulated.

The lateral and top boundaries of the domain were no-flow boundary conditions. The elements located within the drift were simulated as seepage boundaries with zero capillary pressure (i.e., the liquid and gas pressure is always maintained at atmospheric pressure). Therefore, until enough pressure head builds up above the drift, it will serve as a capillary barrier to liquid flow.

The bottom boundary was specified as gravity-drainage flow (i.e., no capillary-pressure gradient). In TOUGH2 v. 1.6, this boundary condition is applied by specifying the name of the material for the bottom boundary as "DRAIN."

Table 2. Summary of injection rates for simulations.

Aperture (microns)	Low Injection Rate per Port (mL/min)	High Injection Rate per Port (mL/min)
100	0.01	0.12
250	0.01	0.24
500	0.01	0.13

IV. RESULTS AND DISCUSSION

IV.A. Distribution of Outflow

The outflow at the bottom of the domain was collected in bins corresponding to the five collection bins used in the experiments. The flow in each bin was normalized to the total amount of flow that would have been collected if the flow were uniform (i.e., total inflow/5). Figure 4 shows the results of the experiments and simulations for different apertures and flow rates.

Both the data and simulation results show that the drift-shadow effect is apparent at larger fracture apertures (250 and 500 microns). The simulations predict the least amount of outflow beneath the drift (Bin 1) with gradually increasing outflow away from the drift in all cases, with more pronounced effects for larger apertures. The impact of flow rate on the simulated outflow distribution was negligible. In all simulations, the contribution to the outflow from the matrix was negligible, and nearly all of the outflow and diversion occurred within the fracture continuum. The saturation was nearly uniform throughout the matrix continuum at a value close to one. A representative simulated flow pattern and saturation distribution in the fracture continuum is presented in Figure 5.

For smaller fracture apertures (i.e., 100 microns), the stronger capillary pressure within the fracture pulled (wicked) more of the water that was diverted around the drift to locations beneath the drift. This general trend in the data (greater outflow directly beneath the drift for smaller apertures) is captured by the simulations, but the overall distributions of the outflow are quite variable in the data. In general, the data show that the outflow far from the drift (Bin 5) is less than in regions closer to the drift, whereas the simulated results show that the outflow continues to increase further from the drift.

The discrepancy between the observed and predicted outflow distribution could be due to heterogeneities and asperities in the experimental fracture that were not captured in the model. These heterogeneities could preferentially direct flow to different regions.

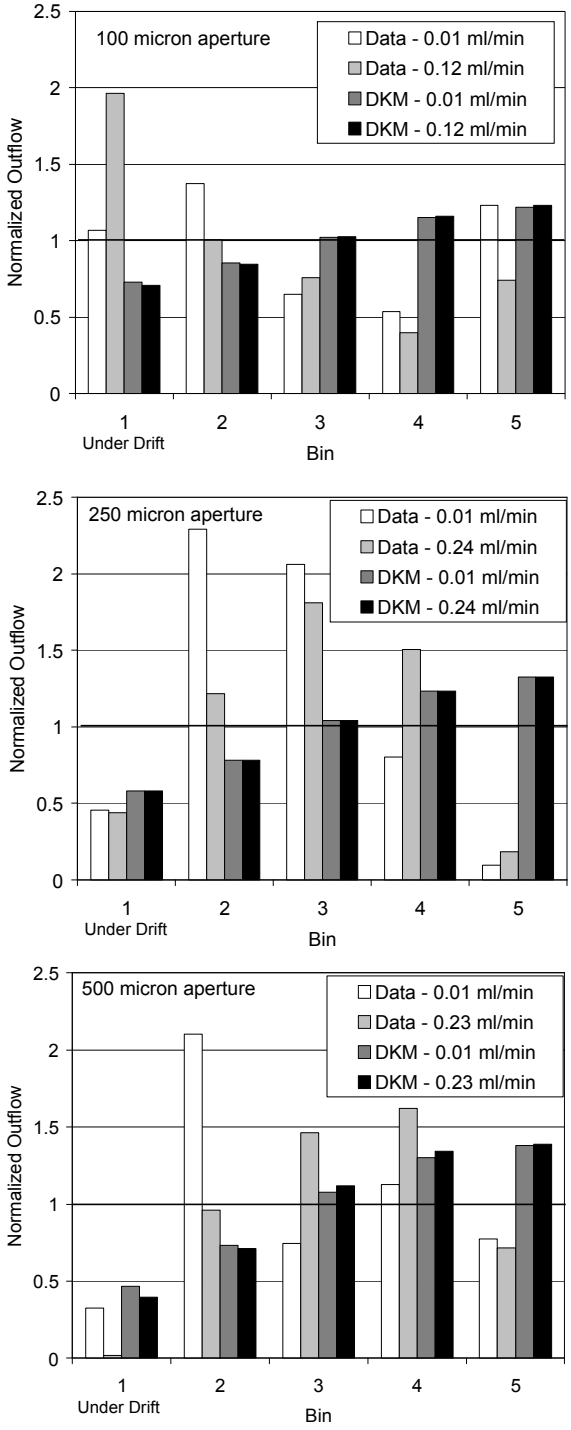

Figure 4. Distribution of normalized outflow below the drift for different fracture apertures and flow rates (DKM = dual-permeability model).

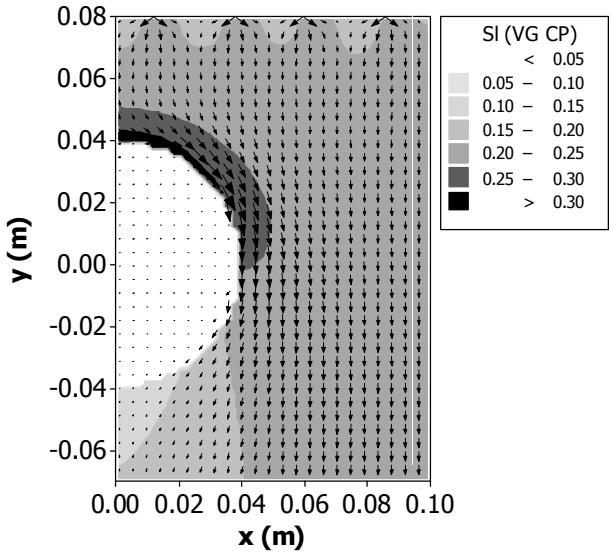

Figure 5. Simulated fracture saturation and flow vectors using TOUGH2 with a 500 micron aperture and 0.23 ml/min flow rate using van Genuchten capillary pressure curves with unbounded maximum pressure (10^{10} Pa).

IV.B. Impact of Fracture Capillary Pressure

Another possible explanation for the discrepancy between the simulated and observed outflow distribution far from the drift is that the fracture capillary pressure was too large in the simulations. This is also supported by the comparison between the observed solute flow patterns in the experiments (Figure 2), which were more discrete and finger-like, and the simulated flow patterns (Figure 5), which were more uniform. As a sensitivity study, the capillary pressure of the fracture continuum was modified to be a linear function of liquid saturation with an arbitrarily low maximum capillary pressure of 30 Pa.

Figure 6 shows the simulated outflow distributions using these small linear fracture capillary functions for the 500-micron aperture test. The simulated results show a non-monotonic outflow as a function of distance away from the drift. In this case, the outflow is concentrated directly beneath the injection ports. The simulated flow pattern using these reduced fracture capillary pressure curves is also more indicative of the observed solute flow paths, which consisted of discrete finger-like flow patterns emanating from the injection ports (Figure 7).

However, the reduced capillary pressures are insufficient to create a capillary diversion around the drift. The simulated flow penetrates through the drift, which is in contrast to the observations of the experiments. Therefore, the optimal fracture capillary pressures to be used in these simulations falls in between the results provided by the van Genuchten parameters and the linear relation used here. At low saturations, the van Genuchten

capillary pressure curve increases to infinity. An arbitrary maximum capillary pressure is often applied, but an improvement may be to use a maximum capillary pressure defined by the Young-Laplace equation (inverse of Eq. (3). The resulting capillary pressures should yield more accurate results in between the bounding results provided here.

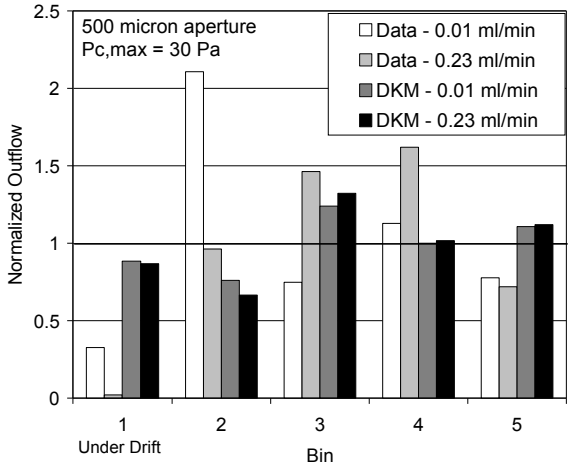

Figure 6. Distribution of normalized outflow below the drift for a fracture aperture of 500 microns using a linear fracture capillary pressure curve with a maximum capillary pressure of 30 Pa (DKM = dual-permeability model).

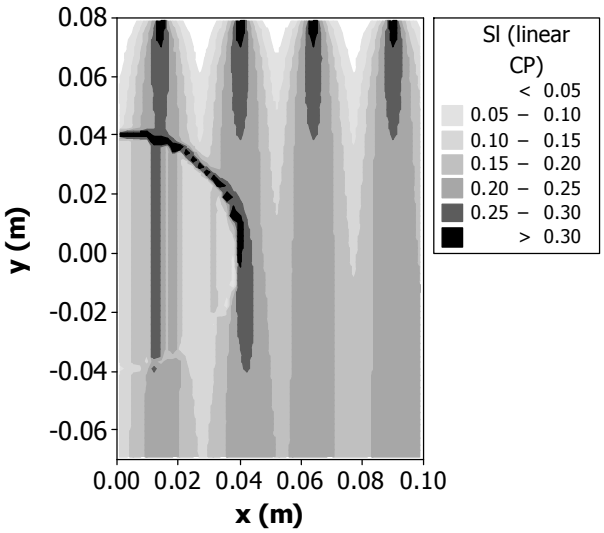

Figure 7. Simulated fracture saturation using TOUGH2 with a 500 micron aperture and 0.23 ml/min flow rate with a maximum linear capillary pressure of 30 Pa.

An intermediate maximum capillary pressure of 200 Pa was applied to the simulations. Figure 8 shows that the trend in the spatial distribution of outflow beneath the drift is more accurately captured using this intermediate capillary pressure. The observed outflow in the experiments is greater in Bins 2, 3, and 4 and less in Bins 1 (under the drift) and 5 (furthest away from the drift). The match between experimental and simulated results is especially good for the 0.23 ml/min case. Figure 9 shows the simulated saturation profile at 0.23 ml/min, which indicates that seepage into the drift does not occur for a maximum capillary pressure of 200 Pa.

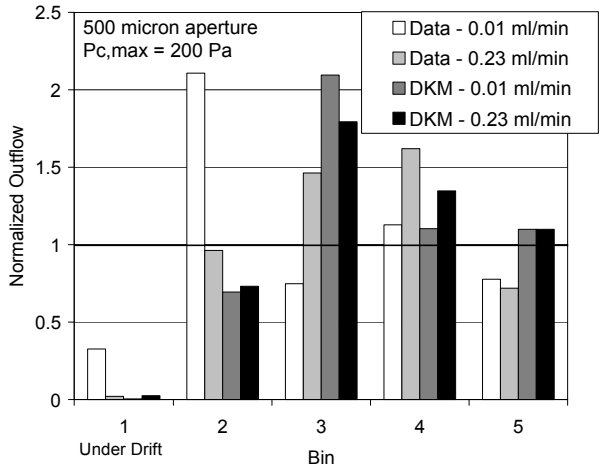

Figure 8. Distribution of normalized outflow below the drift for a fracture aperture of 500 microns using a linear fracture capillary pressure curve with a maximum capillary pressure of 200 Pa (DKM = dual-permeability model).

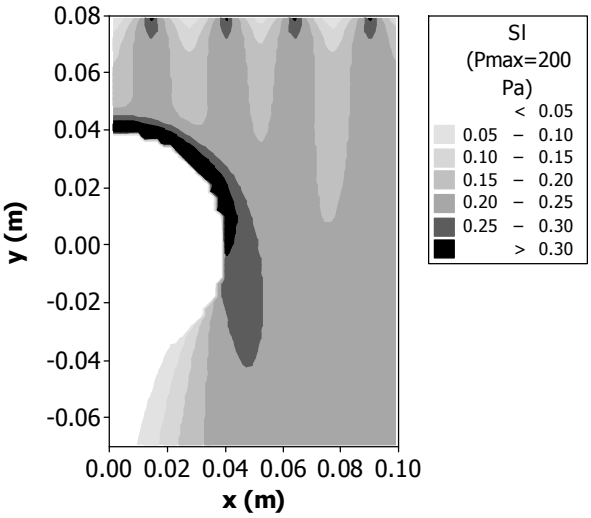

Figure 9. Simulated fracture saturation using TOUGH2 with a 500 micron aperture and 0.23 ml/min flow rate with a maximum linear capillary pressure of 200 Pa.

IV.C. Impact of Mesh

The impact of the mesh on the outflow distribution was investigated using both the orthogonal mesh from the previous simulations and an unstructured mesh shown in Figure 3. The outflow distribution resulting from the different meshes for the 250-micron aperture fracture with a maximum linear capillary pressure of 200 Pa is shown in Figure 10. The results from both meshes are similar at 0.01 and 0.24 ml/min. We originally hypothesized that differences in the seepage and outflow distribution could occur because of the different representations of the curved interface along the drift. The orthogonal mesh represents the drift interface as a stair-stepped connection of elements, whereas the unstructured mesh produces a smooth curved transition between elements (see Figure 3). The impact of this difference will likely depend on the resolution of the mesh. However, for this comparison, the mesh size was sufficiently refined such that no significant differences in the outflow distribution between these two meshes were observed. Seepage into the drift was negligible in both the orthogonal and unstructured mesh.

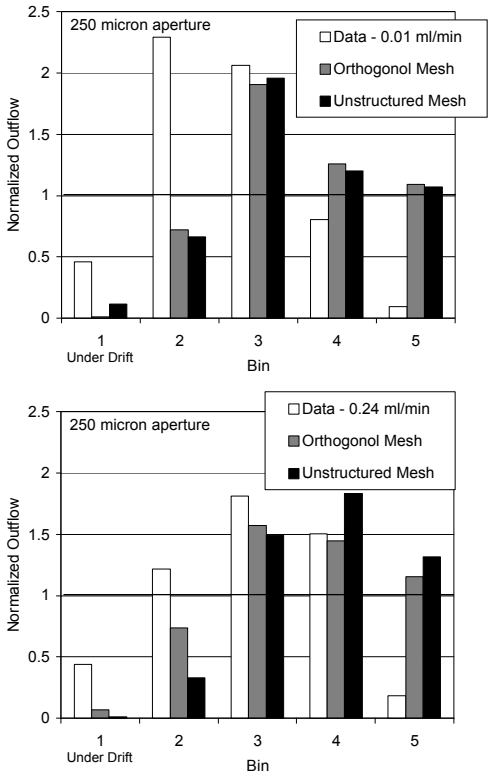

Figure 10. Distribution of normalized outflow using different meshes for a fracture aperture of 250 microns using a linear fracture capillary pressure curve with a maximum capillary pressure of 200 Pa (DKM = dual-permeability model).

V. CONCLUSIONS

Simulations of drift-shadow experiments have been performed to evaluate the impacts of hydrologic properties and mesh design on simulated results. Comparisons with experimental data show that the phenomena of capillary diversion and drift shadow can be represented by the dual-permeability models, although the exact distribution of flux beneath the drift depends on the magnitude of the fracture capillary pressure. Van Genuchten capillary pressure curves with an unbounded maximum capillary pressure yielded more uniform fluxes as compared to the finger-like patterns observed in the experiments. Linear capillary pressure curves with a smaller maximum capillary pressure of 200 Pa yielded better matches to the observed data, but at a maximum capillary pressure of only 30 Pa, the results allowed too much seepage into the drift. Comparisons between the orthogonal and unstructured meshes yielded similar results for the outflow distribution.

ACKNOWLEDGMENTS

Sandia is a multiprogram laboratory operated by Sandia Corporation, a Lockheed Martin Company for the United States Department of Energy's National Nuclear Security Administration under contract DE-AC04-94AL85000.

REFERENCES

1. ALTMAN, S.J., A.A. FORSBERG, W.J. PEPLINSKI, and C.K. HO, "Experimental observation of the drift shadow effect using X-ray absorption imaging," *J. Hydrology*, 348, 341-349 (2008).
2. PHILIP, J.R., J.H. KNIGHT, and R.T. WAECHTER, "Unsaturated Seepage and subterranean holes: conspectus, and exclusion problem for circular cylindrical cavities," *Water Res. Research*, 25(1), 16-28 (1989).
3. HOUSEWORTH, J.E., S. FINSTERLE, and G.S. BODVARSSON, "Flow and transport in the drift shadow in a dual-continuum model," *J. Contaminant Hydrology*, 62-63, 133-156 (2003).
4. SNL (Sandia National Laboratories), "UZ Flow Models and Submodels," MDL-NBS-HS-000006 REV 03 AD 01, Las Vegas, NV (2007).
5. HO, C.K., "Models of Fracture-Matrix Interactions During Multiphase Heat and Mass Flow in Unsaturated Fractured Porous Media," SAND97-1198C, in Proceedings of the ASME Fluids Engineering Division, FED-Vol. 244, pp. 401-412 (1997).

6. PRUESS, K., “TOUGH2—A General-Purpose Numerical Simulator for Multiphase Fluid and Heat Flow,” *LBL-29400*, Lawrence Berkeley Laboratory, Berkeley, CA (1991).
7. ZYVOLOSKI, G.A., B.A. ROBINSON, Z.V. DASH, AND L.L. TREASE, 1995, “Users Manual for the FEHMN Application,” *LA-UR-94-3788*, Los Alamos National Laboratory, Los Alamos, NM.
8. FLINT, L.E., “Physical and hydraulic properties of volcanic rocks from Yucca Mountain, Nevada,” *Water Resources Research*, 39(5), 1119, (2003).
9. ALTMAN, S.J., B.W. ARNOLD, R.W. BARNARD, G.E. BARR, C.K. HO, S.A. MCKENNA, R.R. EATON, “Flow Calculations for Yucca Mountain Groundwater Travel Time (GWTT-95),” SAND96-0819, Sandia National Laboratories, Albuquerque, NM (1996).